https://doi.org/10.5194/egusphere-2026-1579
Preprint. Discussion started: 15 June 2026
© Author(s) 2026. CC BY 4.0 License.

A Cubesat-optimized Magnetic Field Measurement Concept for Operation Beyond Low Earth Orbit

Raphael Steinhöfler[1], Marius Anger[2], Roman Shalamov[2], Jaan Praks[2], David Fischer[1], Werner Magnes[1], Josef Wilfinger[1], Aris Valavanoglou[1], and Constant Lentz[1]

[1]Space Research Institute, Austrian Academy of Sciences, Schmiedlstraße 6 AT-8042 Graz, Austria
[2]Department of Electronics and Nanoengineering, Aalto University, Maarintie 8 FI-02150 Espoo, Finland

Correspondence: Raphael Steinhöfler (raphael.steinhoefler@oeaw.ac.at)

Abstract. This paper presents a CubeSat-optimized measurement concept for magnetic field, which was designed for missions beyond low Earth orbit targeting novel radiation belt studies. The instrument combines a miniaturized three-axis fluxgate sensor on a low-mass deployable boom together with a compact sensor control unit that implements fully synchronous excitation, sampling, and digital control. A hybrid feedback module integrates three prototype fluxgate feedback microchips that provide low-noise current sources with selectable full-scale ranges ($\pm 3/\pm 9\ \mathrm{mA}$), enabling vector measurements over $\pm 70\ \mu\mathrm{T}$ while retaining sub-nT resolution. The boom provides 65 cm standoff from the CubeSat and pointing knowledge of 1°. The designed boom length limits the tolerable magnetic dipole moment inside the CubeSat to 0.05 Am^2. Extended housekeeping includes voltage supply and thermal monitoring, an additional magneto-inductive sensor on the sensor control unit for disturbance discrimination, and total ionizing dose tracking. Laboratory characterization demonstrates noise densities of 20–30 $\frac{\mathrm{pT}}{\sqrt{\mathrm{Hz}}}$ at 1 Hz, with 128 vectors per second science data and linearity suitable for near-Earth fields. As it is a pivotal element in the instrument, the prototype feedback microchip was tested for its radiation response. Heavy-ion testing showed no single-event latch-up up to 100 $\frac{\mathrm{MeV\ cm}^2}{\mathrm{mg}}$. Single-event transients as well as single-event upsets were observed and are consistent with rare functional interrupts in the digital part of the signal chain. They are addressable by standard redundancy techniques. X-ray tests up to 1 Mrad confirm functionality with worst-case gain and offset drifts of approximately 600 $\frac{\mathrm{ppm}}{\mathrm{krad}}$ and 1 $\frac{\mu\mathrm{A}}{\mathrm{krad}}$ within 0–100 krad. The prototype meets the performance requirements derived from the Foresail-2 mission concept and demonstrates a path to high-quality, resource-efficient magnetometry on 3U–6U CubeSat platforms suitable for operation in the Van Allen belts and other harsh radiation environments.

1 Introduction

Magnetic field data deliver a wealth of information about geophysical, space plasma, and solar phenomena and are therefore highly in demand for various scientific disciplines. The demand for such measurements meet a recent development for scientific space missions, that tend to operate on increasingly smaller satellite platforms. These missions benefit from the availability of space launch providers that offer solutions accessible to small institutions and research groups. Furthermore, highly-populated, multi-satellite constellations become more important for the advancement of various scientific fields, e.g. the time resolution to investigate dynamic high-energy particle phenomena in the Earth's magnetosphere is enabled by a constellation like the proposed CORBES mission (Wu et al., 2025).

Current developments in CubeSat magnetometers feature small form-factor solutions like the magnetoresistive magnetometer aboard the RadCube (Eastwood et al., 2025) or the fluxgate magnetometer aboard the Ex-Alta 1 satellites (Miles et al., 2016). While these developments demonstrate the principles of space magnetometry, they do not fully exploit the potential possibilities.

In order to further explore CubeSat concepts and to push the capabilities of future missions, especially in the radiation belts, a miniaturized fluxgate magnetometer prototype was developed by the Space Research Institute of the Austrian Academy of Sciences in cooperation with the Department of Electronics and Nanoengineering of Aalto University. This technological study aims to improve on existing concepts in several domains, including but not limited to the reduction of the noise floor in the magnetic field measurement, the enhancement of the mechanical stability of the boom system, and enabling greater awareness of disturbances such as noise generated by the spacecraft itself and radiation-induced performance degradation.

Electronic operation of the fluxgate magnetometer prototype is provided by a dedicated module, incorporating decades-long expertise in magnetometry as well as recent developments in application-specific integrated circuits designed for fluxgate front-end electronics. The instrument utilizes a small form-factor sensor built by LEMI LLC (Forslund et al., 2007). A novel aluminum boom was designed and developed to operate in this specific setup. It holds the sensor and fits a 3U or 6U CubeSat.

The sensor itself uses the fluxgate principle, which periodically drives a soft-magnetic ring core into saturation using an excitation signal. A secondary sense coil wound around the entire ring core is used to pick up a signal that contains harmonics of the excitation frequency. The presence of an external magnetic field causes an asymmetry in the saturation depth and introduces even harmonics in the pick-up coil which are proportional to the magnetic field. These even harmonics are minimized by a tertiary feedback coil that generates a magnetic field that opposes the concentrated ambient field inside the ring core. Through the application of a control loop and evaluation of the feedback current, the ambient magnetic field is measured with high linearity and precision. The whole assembly is constructed in the same way for each spatial axis, enabling measurement of the magnetic field vector.

In an effort to further minimize the volume, weight and number of electronic components needed for a fluxgate magnetometer and to improve on noise and linearity figures as well as radiation tolerance, an application-specific integrated circuit was developed in cooperation with Graz University of Technology (Scherzer et al., 2022). This integrated circuit incorporates all modules needed to convert a digital output value to an analog current and to amplify it to different ranges.

The fluxgate magnetometer described in this work was built to meet the requirements of the proposed Foresail-2 mission as part of the CORBES constellation (Anger et al., 2023; Wu et al., 2025). The Foresail-2 mission is designed as a model for operations in harsh environments, and the development of its magnetometer reflects this focus on resilience and adaptability, making it suitable for a wide range of other missions. Furthermore, crucial tests of performance and radiation hardness parameters pivotal to the operation in the model mission profile were performed, demonstrating the technology's readiness for space.

https://doi.org/10.5194/egusphere-2026-1579
Preprint. Discussion started: 15 June 2026
© Author(s) 2026. CC BY 4.0 License.

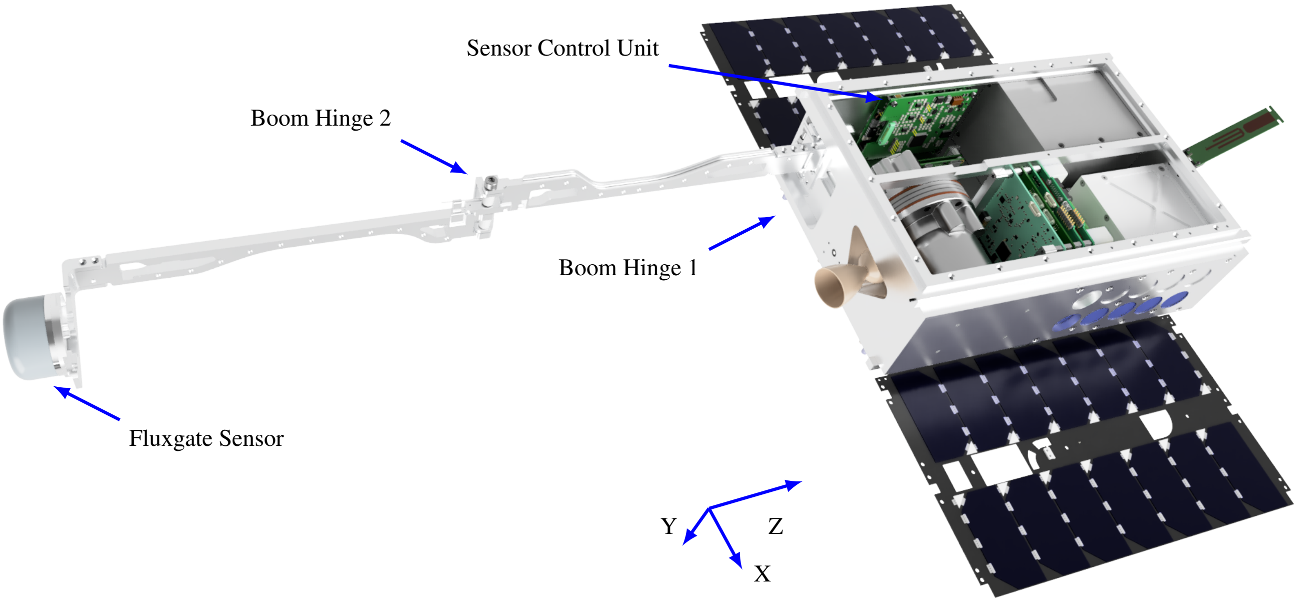

Figure 1. The planned Foresail-2 satellite with a deployed boom and all components of the instrument highlighted. Bottom panel removed for illustration purposes. The MAST boom is extending towards the Z-direction.

2 Instrument Design

The magnetometer was designed to be integrated into a radiation shielded 6U CubeSat such as the planned Foresail-2 mission and includes the fluxgate sensor, sensor boom, harness and the read-out electronics. Figure 1 shows a rendering of the instrument installed on the satellite in its measurement configuration with deployed boom.

The block diagram in Figure 2 shows how the sensor is connected to the Sensor Control Unit (SCU) via the harness running along the boom. In the SCU, a single excitation driver and resonator is used to drive the soft magnetic cores of all three axes. The analog front-end for operating the sensor is formed by an amplifier and Analog-to-Digital Converter (ADC) for the sense path and a fully-integrated prototype feedback ASIC which integrates a current Digital-to-Analog (DAC) converter and a current amplifier. All the front-end ADCs and DACs sampling frequencies as well as the excitation signal are precisely and synchronously timed by a Field-Programmable Gate Array (FPGA). This FPGA implements all the digital logic that closes the control loop of each axis and provides the interface to the spacecraft. The interface also facilitates the configuration of instrument parameters and the read-out of measured data. In addition to the classic housekeeping functions like voltage, current, and temperature monitors, a Total-Ionizing-Dose (TID) monitor and a low-precision magneto-inductive magnetometer are integrated in the SCU. These extended housekeeping functions enable data evaluation capabilities unprecedented in small

© Author(s) 2026. CC BY 4.0 License.

satellite magnetometers. Furthermore, the fully reconfigurable digital logic provides a multitude of operational modes ranging from open loop sensing to closed loop feedback in different ranges.

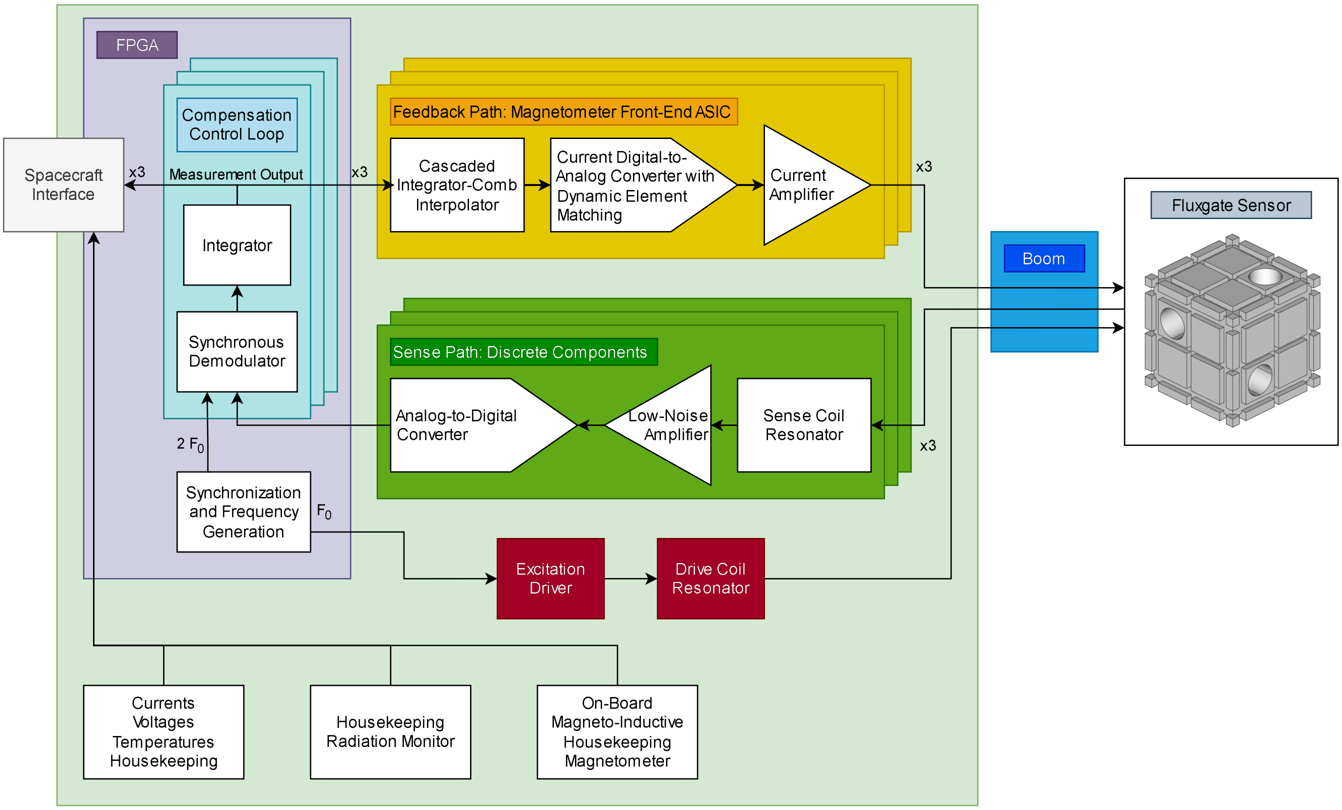

Figure 2. Block diagram of the instrument

2.1 Sensor

75 To ease integration of the magnetometer instrument into a 6U CubeSat, a miniaturized sensor developed by Forslund et al. (2007) is used. It consists of a macor carrier cube with a low coefficient of thermal expansion (CTE). The carrier cube has a side length of 20 mm and machined groves for the feedback coils as well as the soft-magnetic cores. Each axis features two cores of soft-magnetic material in a double-rod configuration instead of the classic ring core commonly used by fluxgate sensors in space (Balogh, 2010). These two rods are placed into a cylindrical spool assembly on which the sense coil is wound. Each axis' assembly is placed slightly off-center to not cross the assembly of the other axes. Although this design does not expose the soft-magnetic cores to the most homogeneous field region of the feedback coil system, it provides excellent manufacturability and leaves the option to change the magnetic cores even when the sense and feedback coils are already wound onto the cube. Feedback is provided by two parallel coils wound in the outermost possible positions and a third coil in the middle of each axis. The three-coil arrangement is a trade-off between manufacturability and field homogeneity inside the cube. Furthermore,

© Author(s) 2026. CC BY 4.0 License.

to provide a solder-able connection to the coils of the sensor, a printed circuit board holding solder pads is attached on one side of the sensor cube. Figure 3 shows the cube mounted on a mockup baseplate including the connection wires soldered to the pads on top. A PT1000 thermistor is mounted on the backside of the sensor to measure the temperature of the carrier cube and eventually compensate measured data for effects caused by thermal expansion or contraction of the carrier cube. The sensor cube itself has a mass of less than 20 g and features a magnetic noise density at 1 Hz below 30 $\frac{\mathrm{pT}}{\sqrt{\mathrm{Hz}}}$. The sensitivity of the sense coils is at 5 to 12 $\frac{\mu\mathrm{V}}{\mathrm{nT}}$ and the feedback coil constant is at 7.5 to 7.9 $\frac{\mathrm{nT}}{\mu\mathrm{A}}$. The deviation from orthogonality between the axes is below 0.5°.

Figure 3. Miniaturized fluxgate sensor mounted on a mockup baseplate (Forslund et al., 2007). Harness connections are soldered to a PCB mounted on top of the sensor cube.

2.2 Boom

To reduce the magnetic stray field from the CubeSat at the position of the magnetic field sensors, they need to be positioned at a significant distance from the spacecraft body. In order to meet the measurement requirements while allowing a dipole moment of 0.05 Am^2 inside the spacecraft, a boom length of at least 50 cm is required. Additionally, the relative orientation of the sensor head to the spacecraft and to the geophysical reference system needs to be known with an accuracy of 1° or better to be able to deliver a precise science product, so that the attitude requirement of the Foresail-2 specification (Anger et al., 2023) is fulfilled. Variable disturbances shall be minimized, and the spacecraft operations may need to be adjusted accordingly.

To achieve the required sensor distance to the CubeSat body, deployable booms are commonly used. Typically, used concepts include tape-spring booms, which provide meter-class standoff with very low mass but can exhibit snap-through and long settling times if not damped (Vitztum et al., 2019; Eastwood et al., 2025). Other concepts incorporate segmented telescopic booms, which are structurally simple and compact but likewise require attention to deployment dynamics and vibration ("ringing") for precision magnetometry (Miles et al., 2016).

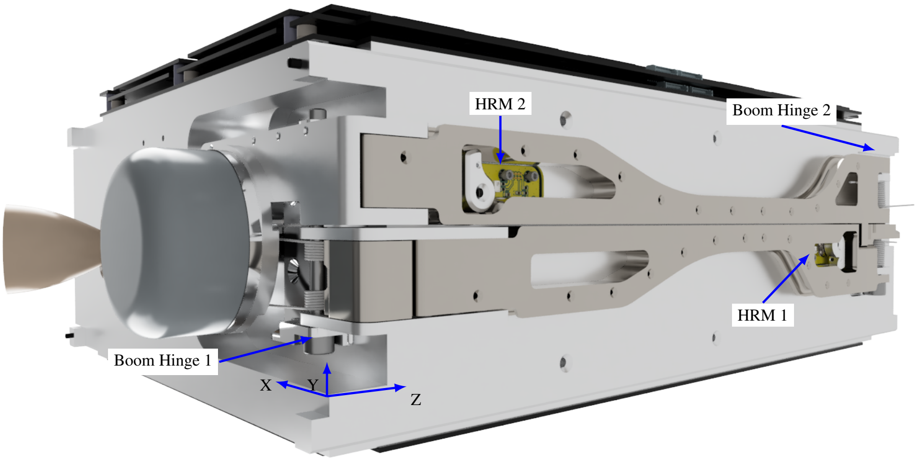

Figure 4. Foresail-2 in stowed configuration. The fluxgate sensor is placed inside the tuna can volume of the 6U satellite. The boom prototype extends 10 mm into the allowed external space of a CubeSat. Two Hold and Release Mechanisms (HRMs) are securing the two arms of the folding boom.

As the body of a 6U CubeSat is limited in volume, a rigid boom with two folding arms has been chosen in the preliminary design study (Anger et al., 2023). One long side of the spacecraft as well as one tuna can space was available for use. The designed boom prototype is shown in its stowed position on the side of the spacecraft in Figure 4. The boom deploys twice around two axes by 180° each. The deployment is initiated and observed by a Hold and Release Mechanism (HRM) for each arm. A top view for one of the HRMs is shown in Figure 5.

It uses a simple burn wire mechanism, which holds a spring actuated rotation arm. The HRMs also provide information about a successful deployment via mechanical switches.

Additionally, each arm is locked in place after deployment.

The boom also needs to accommodate the harness from the Sensor Control Unit (SCU) inside the spacecraft to the magnetometer sensor. The sensor head is connected to the SCU via a harness comprising UV-protected twisted pair cables covered by an aluminum braid. The harness is securely fixed on the outside of the boom arms with Dacron strings, as seen in Figure 6. It rests inside a groove that runs along each arm. The harness is routed underneath the boom structure at the second rotation axis. This enables the overall envelope of the geometry to remain inside the limit of 10 mm above the 6U CubeSat specifications, maintaining the CubeSat standard (The CubeSat Program, 2022).

The boom is constructed from lightweight, non-magnetic materials. The arms and other structural parts are made of Aluminum 7075. All screws and springs are made of TC4 Titanium. The interfaces between moving parts are either separated by Polyether Ether Ketone (PEEK) washers or comprised of two different materials (e.g. Al and Ti) to prevent cold welding is-

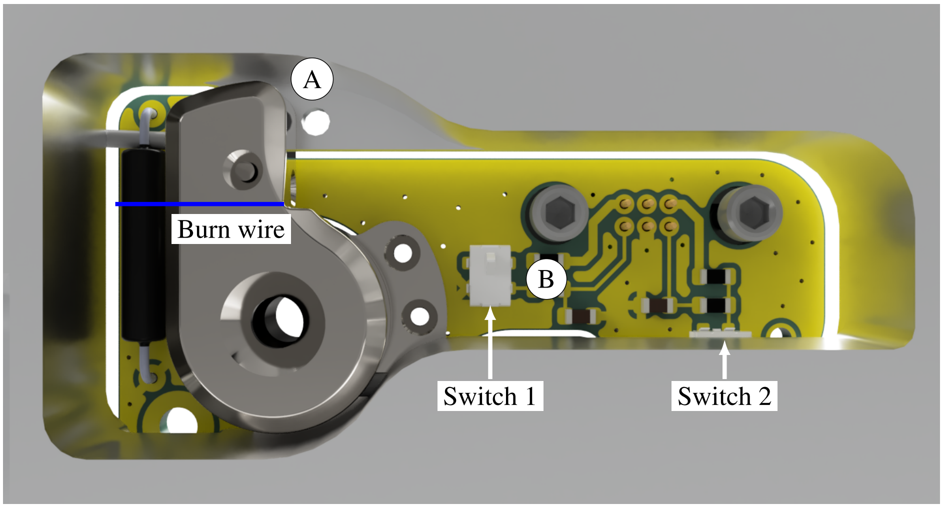

Figure 5. Boom hold and release mechanism prototype. The rotation arm on the left is stowed in position A and unlocked in position B. The arm is held in place by a burn wire across the resistor on the far left. Switch 1 indicates the successful release of the arm, while Switch 2 confirms the deployment of the respective boom arm.

sues. Thermal simulations of the boom and sensor structure have shown that the sensor head can be kept within 10 to 60 $^\circ\mathrm{C}$ for operation in low and medium Earth orbit, as outlined by the Foresail-2 mission profile (Raman, 2023). The thermal interface can be adjusted to the mission needs by adding a PEEK insulation plate between the boom and the sensor head.

The boom itself has a weight of about 202 g and the harness together with the sensor head weighs around 135 g. Each hold and release mechanism has a mass of 6 g. This brings the total mass of the mounted boom on the satellite to about 350 g.

2.3 Sensor Control Unit

The SCU depicted in Figure 1 and Figure 7 is miniaturized into a very small form factor (92 mm × 85 mm × 25mm), while comprising all electronics that are needed to operate the fluxgate sensor. Besides the excitation circuit and sense coil amplifiers, it integrates the purpose-built hybrid prototype feedback ASIC that is used to compensate the ambient field. Furthermore, a Field-Programmable Gate Array (FPGA) that operates the control loop and a multitude of housekeeping functions are designed into the SCU, providing awareness of the state of the instrument, potentially optimizing the data quality of the instrument.

All digital electronics of the instrument operate on tightly synchronized timing signals generated from a single clock source. This ensures that no undesired self-generated intermodulation products disturb the measurement signal.

The three series-connected excitation coils of the sensor are wired in parallel to a capacitor, forming a resonant excitation circuit that provides a well-saturating magnetic field waveform suitable for the sensing application. This resonant circuit is driven by a MOSFET H-bridge connected via a series inductor. An optimal resonance condition (Forslund et al., 2007) is achieved through tuning the resonance capacitor, series inductor and supply voltage of the circuit. Additional tuning was applied after closing the feedback loop to obtain a low noise floor.

https://doi.org/10.5194/egusphere-2026-1579
Preprint. Discussion started: 15 June 2026
© Author(s) 2026. CC BY 4.0 License.

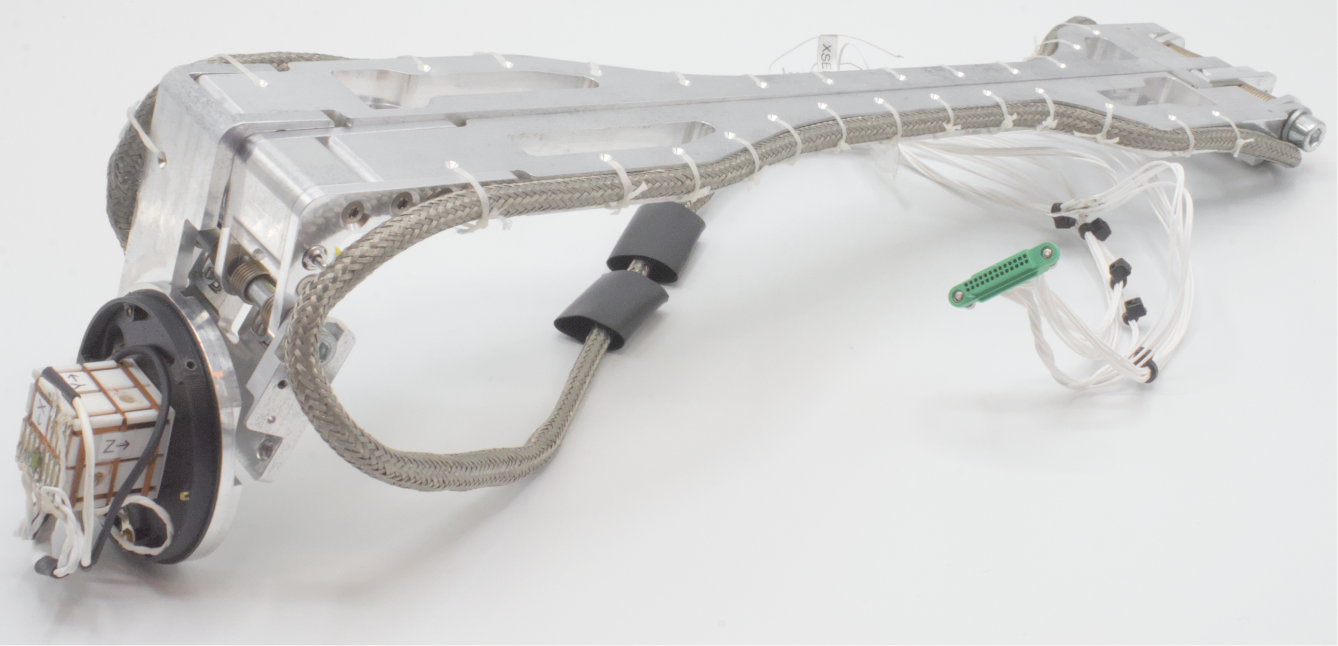

Figure 6. Boom assembly seen from the side. The sensor head on the left shown without the protective cover.

On the sense side, a parallel capacitor and resistor is added to each pick-up coil, forming a damped resonant circuit. It is tuned to optimally output the even harmonics of the excitation frequency f_0 that correspond to the external magnetic field. In particular, the output signal of the 2 f_0 harmonic is maximized and used for the control loop of the fluxgate (Ripka, 1992).

This sense signal is amplified by a Low-Noise Amplifier, processed by additional analog filters and digitized by an ADC. All of the analog signal path is implemented using differential signals to minimize any potential common-mode interference present in the satellite. The sampling of the sense signals happens at an exact phase relation to the excitation signal. Synchronous demodulation is accomplished by sampling the input four times during one excitation period, inverting every other sample and summing all samples. This method sets the minimum sampling rate required for the controller and eliminates the need for a matched filter to extract the even harmonics (Auster et al., 2008). An integrating controller is fed by the demodulated sense input, which acts as the error signal. The output signal of the controller is used to update the feedback coils at 4 f_0, completing the control loop and minimizing the field inside the sensor along each axis. The actual measurement value is a filtered and downsampled version of the feedback signal. The actual output of the feedback currents for all three axes is provided by a hybrid integrated circuit which combines three identical feedback ASIC dies into one package. Data transmission from the FPGA to the feedback ASIC dies operates in a differential mode with a signal voltages as low as 320 mV, thereby minimizing digital interference.

The sensor's feedback coils are connected directly to the output of the prototype feedback ASIC. An additional 10 µF ceramic capacitor across each of the feedback coils is connected to limit the bandwidth of the output. With a current output range of

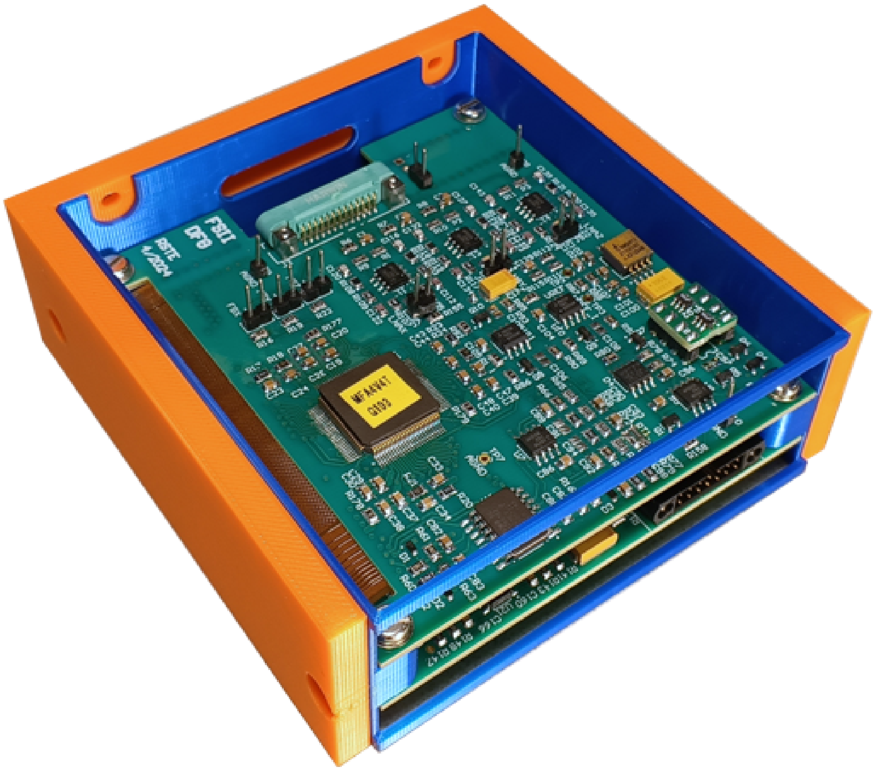

Figure 7. The sensor control unit of the instrument mounted in a satellite bus mockup.

$\pm$ 9.1 mA and a coil factor of the sensor of 7.7 $\frac{\mathrm{nT}}{\mathrm{\mu A}}$, a measurable field range of $\pm$ 70070 nT is possible. With this range, the instrument is suitable for near-earth missions that experience the full magnitude of the Earth's magnetic field. However, as explained in subsection 2.4, a lower range, with a higher sensitivity and a better noise figure can be achieved using a lower current output mode of the prototype feedback ASIC.

Figure 8 shows the spacecraft interfaces required by the SCU. A regulated 5 V line powers both the digital and analog front-end electronics. Furthermore, an unregulated 8 V line is needed by the analog front-end electronics for the operation of the sensor drive circuit as well as the current and radiation monitors.

A custom protocol based on the EIA-485 standard for communication is used as command and data interface between the spacecraft and the instrument. The cold redundant system comprises a main and redundant bus. Each bus uses a fault-protected UART to RS-485 half duplex transceiver. Selection of the active bus is done by the Oboard Data Handling Subsystem (OBDH) at startup and the SCU responds accordingly.

2.4 Prototype Feedback Application Specific Integrated Circuit

The most crucial part in the signal chain is the output DAC that delivers the high-precision feedback current. It determines the resolution, noise, thermal, and linearity characteristics of the measurement. A specialized prototype feedback ASIC was

© Author(s) 2026. CC BY 4.0 License.

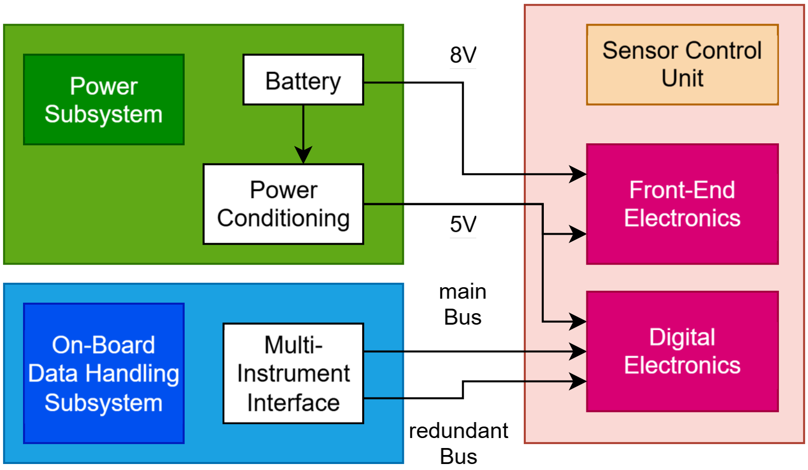

Figure 8. Block diagram of the electrical spacecraft interfaces

170 developed in cooperation with the Institute for Electronics of Graz University of Technology (Scherzer et al., 2022) to improve on the aforementioned quality parameters. Figure 9 shows three identical feedback ASIC dies packaged together to provide all feedback currents for a three-axis fluxgate instrument.

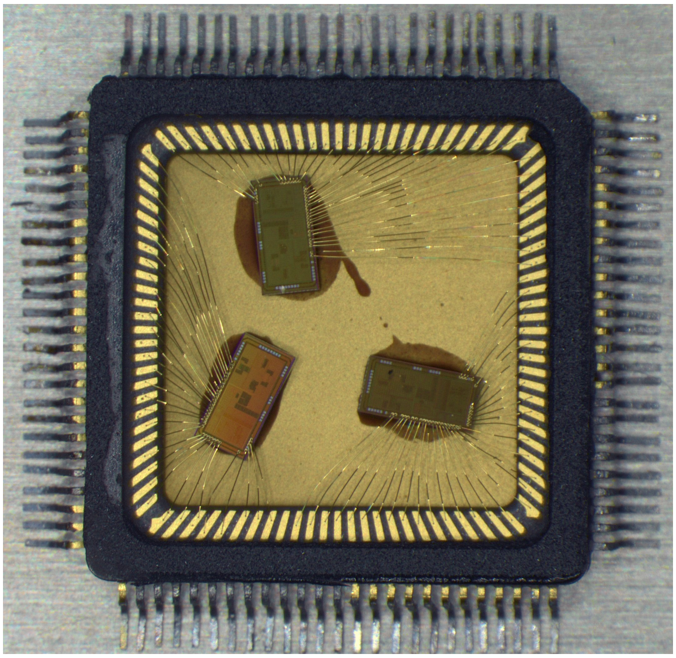

Figure 9. Three prototype feedback ASICs bonded in a 100-pin ceramic package, forming a vector feedback chip

https://doi.org/10.5194/egusphere-2026-1579
Preprint. Discussion started: 15 June 2026
© Author(s) 2026. CC BY 4.0 License.

Feedback current is provided by a specialized modulator and amplifier topology. The DAC utilizes a Cascaded Integrator-Comb interpolator (CIC) to handle necessary conversions of sampling rates and bit-widths. This CIC interpolator is followed by a combination of a high and low range signed 4-bit Δ/Σ modulator as shown in Figure 10. The modulated signals are fed into a matched current cell array, summing the coarse and fine current signal. A special technique called Dynamic Element Matching (DEM) is employed to minimize nonlinearities caused by mismatch of the individual cells with randomly selecting the cells that are used. While the linearity of the output signal is strongly improved by DEM, tones with an amplitude of up to 2.3 nT are added to the output when measuring DC fields. In order to amplify the summed output of the current steering cells to a usable level, a fully-differential amplifier in a Howland current-controlled current source configuration is used (Scherzer and Auer, 2022). This integrated current amplifier allows configuring two different current output ranges, one at 3 mA and one at 9 mA full-scale range. Consequently, the ASIC covers a broad range of sensors and applications in space exploration.

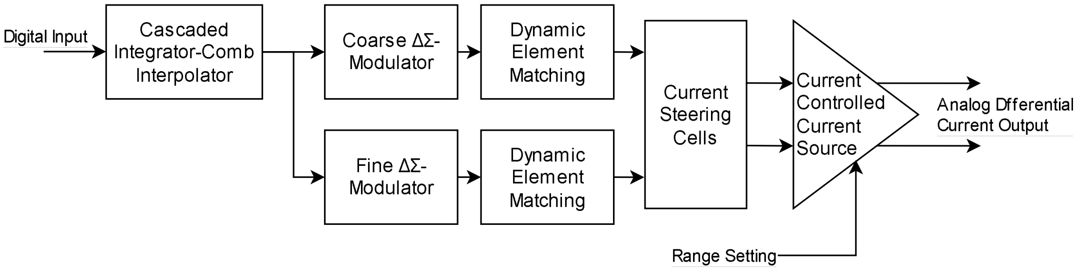

Figure 10. Block diagram of the prototype feedback ASIC

2.5 Housekeeping

In order to gain awareness of the overall state of the instrument, a multitude of housekeeping data is acquired.

Voltage and current are monitored on both 5 V and 8 V power supply channels. In addition, the supply current of the prototype feedback ASIC is measured seperately and provides a coarse estimate of the field magnitude that is registered by the instrument.

For both the sensor and the SCU, a PT1000 thermistor provides a measurement of their temperature. The read-out circuits of the thermistors enable a theoretical temperature range of $\vartheta_{min} \approx -110\ ^{\circ}C$ and $\vartheta_{max} \approx 185\ ^{\circ}C$ with a sensitivity of 0.073 $\frac{\mathrm{K}}{\mathrm{LSB}}$.

In addition to the voltage, current and temperature monitoring channels, the miniature magneto-inductive magnetometer sensor RM3100 (Regoli et al., 2018) is added to the SCU. Similar to an inboard sensor that is mounted on a magnetometer boom closer to the spacecraft, typical in larger missions, this housekeeping magnetometer is situated directly inside the spacecraft electronics. With it, it is possible to identify magnetic disturbances caused by the spacecraft's subsystems. While the external magnetic flux density that should be measured is uniform over spacecraft scale, a disturber situated on the spacecraft generates a measurable field gradient (Constantinescu et al., 2020). The additional localized flux density measurement allows the determination of a field gradient that is used to separate the spacecraft noise from the background field. This technique enables

© Author(s) 2026. CC BY 4.0 License.

more sophisticated data cleaning and post-processing resulting in a very high quality data product.

As the intended operational orbit of this instrument covers the Van Allen radiation belts, a nominal ionizing dose of up to 100 krad is expected over its lifetime. In order to verify the actual radiation dose, two RADFETs (Holmes-Siedle and Adams, 1986) are added to the housekeeping capabilities of the instrument. These specialized and calibrated P-channel MOSFETs provide information on the Total Ionizing Dose (TID) experienced by the spacecraft. When operated in an ideal-diode configuration driven by a defined bias current, the source-to-drain voltage changes with applied TID. The TID is related to the voltage change via a second-order polynomial without a constant coefficient, the exact values of which are provided by the manufacturer's calibration.

With typical coefficients given, a minimum sensitivity of approximately $0.1\,\frac{\mathrm{krad}}{\mathrm{LSB}}$ is achieved. For the manufacturer's calibration to be valid, a timed routine for exposure and read-out of the RADFET is required. In this routine, when the RADFET is not read out, all terminals of it are grounded to prevent any charge accumulation that is not related to the TID.

2.6 Resource Specification

To a spacecraft designer, several parameters such as volume, mass, power consumption and maximum data rate of the instrument are pivotal for the overall spacecraft design. A specification of all these parameters is given in Table 1. It lists the outer dimensions and masses of each subsystem of the instrument.

Table 1. Mass and volume of the instrument and its subsystems

subsystem	length mm	width mm	height mm	volume cm^3	mass g
Sensor Control Unit	92	85	25	195.5	80
Boom	650 (deployed length)			-	215
Sensor and cap	54	54	29	66.42	35
Harness	-	-	-	-	100
total	-	-	-	-	430

For electrical power consumption, a detailed listing of the current draws of the subsystems of the SCU is given in Table 2. Furthermore, each subsystems power consumption is calculated and summed for the whole instrument.

To a satellite data processing unit, the instrument presents the following data. The data is split into magnetic field data, housekeeping data and communication and synchronization overhead. The magnetic field and housekeeping data may be down-sampled on demand to reduce the required data processing capabilities. Nevertheless, to get a safe number on the requirements, the maximum data rates are given in Table 3.

https://doi.org/10.5194/egusphere-2026-1579
Preprint. Discussion started: 15 June 2026
© Author(s) 2026. CC BY 4.0 License.

Table 2. Electrical power consumption of the instrument and its subsystems

subsystem	voltage domain V	current draw mA	power consumption mW
FPGA and communication	5	66.96	334.8
Magnetometer Front-End ASIC	5	50.7	253.5
Sense Front-End	5	5.85	29.25
Sensor Excitation	5	19.23	153.84
Housekeeping	5	5.41	27.05
Housekeeping	8	3.73	29.84
total 5 V (including losses)		132	660
total 8 V (including losses)		22.96	183.68
total	all	-	843.68

Table 3. Maximum data rates for all data types

data type	description	word width (in packet) Bit	data rate $\frac{\mathrm{kBit}}{\mathrm{s}}$
Magnetic field	X, Y and Z component of the magnetic field	72 * 16	9.216
Housekeeping data	8 rotating housekeeping channels	24 * 16	2.048
Communication overhead	communications protocol handling	72	0.576
Synchronization overhead	synchronization of data	32	0.256
payload	measurement data	1664	11.264
total	full packets including overhead	2040	16.32

https://doi.org/10.5194/egusphere-2026-1579
Preprint. Discussion started: 15 June 2026
© Author(s) 2026. CC BY 4.0 License.

3 Tests and Results

In order to get an overview of the capabilities and to assess the readiness of the SCU for an actual space mission, several tests have been carried out. These tests include a noise analysis of the whole system and the contribution of the prototype feedback ASIC, an evaluation of control loop tuning parameters, thermal response of the SCU and a thorough radiation evaluation of the prototype feedback ASIC. While these laboratory tests are not representative of the expected performance in space, they capture the performance contributions of all the new developments in this work.

3.1 Instrument Performance

The first version of the instrument has undergone several performance tests, including a determination of noise in a low DC field, and the effect of control loop tuning as well as total harmonic distortion on the measurement result. Furthermore, temperature drifts of the gain and offset calibration parameters were recorded. All the tests were carried out for both, the High Range (HR) and Low Range (LR) mode. A summary of the performance and limits of both ranges is given in Table 4.

Table 4. Performance summary of both measurement ranges

range	B_{max} nT	sensitivity $\frac{\mathrm{pT}}{\mathrm{LSB}}$	noise at 1 Hz $\frac{\mathrm{pT}}{\sqrt{\mathrm{Hz}}}$
High Range	70000	23	≤ 30
Low Range	23000	7.6	≤ 20

The noise floor of all axes for both, the LR and HR mode is given in Figure 11. It is evident in the plots that the noise at 1 Hz is below 30 $\frac{\mathrm{pT}}{\sqrt{\mathrm{Hz}}}$. While the feedback current gain of the HR and LR mode are separated by a factor of ≈ 3, the noise floor is scaled with a lower factor, as seen in the differences between Figure 11a and Figure 11b. This is due to a substantial part of the noise energy being contributed by the sensor itself.

While the sensor's noise floor does not change when switching the measurement range, the noise floor of the electronics is changed. Separation of the electronics and sensor noise is enabled by the knowledge of both, the overall HR and LR noise floor as well as the ratio between the noise contributions of the electronics in both ranges. The relations required for the noise separation are listed in Equation 1 and Equation 2.

$$B^2_{N_{tot,range}}(f) = B^2_{N_{EL,range}}(f) + B^2_{N_{SEN}}(f) \tag{1}$$

$$B_{N_{EL,HR}}(f) = B_{N_{EL,LR}}(f)\frac{A_{HR}}{A_{LR}} \tag{2}$$

As the current feedback is the main noise contributor in the electronics, the ratio $\frac{A_{HR}}{A_{LR}}$ could be determined from noise spectra acquired during tests of the prototype feedback ASIC. This ratio is nearly constant throughout the frequency range

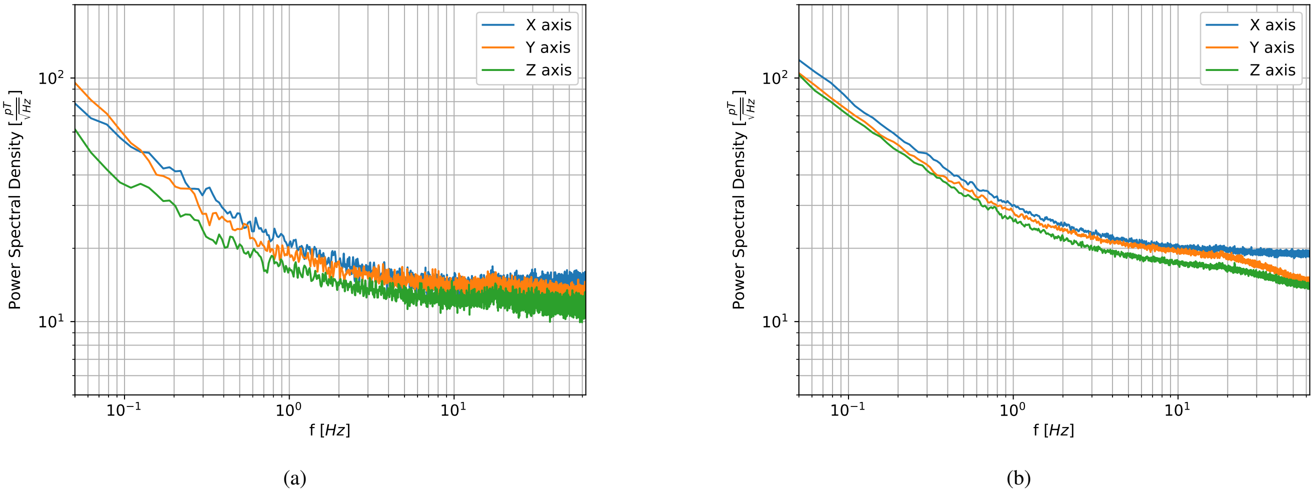

Figure 11. Power spectral density of each axis in a low DC field environment with less than 300 nT. Left: Instrument in LR mode, right: Instrument in HR mode

and facilitates the separation of electronics and sensor noise, with results shown in Figure 12. The noise separation calculation demonstrates that the sensor noise density roughly follows a $\frac{1}{f}$ - characteristic. Above approximately 1 Hz, it is consistent with the reference sensor noise tests performed by Forslund et al. (2007). With lower frequencies, the measured noise density increases less than the reference. Especially at very low frequencies below 100 mHz, the measured noise is less than half of the reference. This phenomenon may be explained by a higher energy used to flip the magnetization of the soft magnetic cores in this design. Overall, the noise spectrum is dominated by the white noise of the SCU above 1 Hz in HR mode, while the LR mode is dominated by the sensor noise.

When the feedback loop is switched on, a control loop comprising an integrator with variable gain is introduced to the signal path. The frequency response of the measurement is highly dependent on the gain K_I applied to the demodulated sense signal that is fed into the integrator. As seen in Figure 13, a distinct first-order low-pass behavior is added within the measurement bandwidth when the integrator gain is low. While the $\frac{1}{f}$-noise from the sensor does not change, the observed low-pass behavior is reminiscent of the actual flux density transfer function. The disturbance recorded at 17 Hz with integrator gains $K_I = 2$ and $K_I = 4$ is likely caused by a disturbance in the generation of the artificial field that the measurements were taken in. However, the exact source of the disturbance remains unresolved.

While the dependency of the measurement offset and gain on the sensor temperature is known (Forslund et al., 2007), the influence of the SCU's temperature was specifically investigated. Figure 14a and Figure 14b show the temperature behavior of all three axes in LR mode. It is noticeable that the offset does not change equally for all axes while the gain deviation appears to be fairly uniform.

As evident in Figure 15b, the offset change is fairly uniform for all three axes in HR mode. While the offset change is comparable to the LR mode, the gain deviation in HR mode is lower for both the X-axis and Z axis. However, the Y axis shows

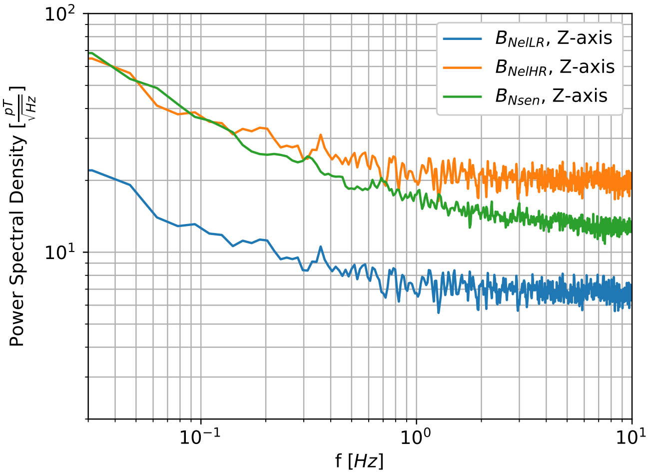

Figure 12. Comparison plot for Z-axis: Sensor noise B_{Nsen}, electronics noise in HR B_{NelHR} and in LR B_{NelLR}

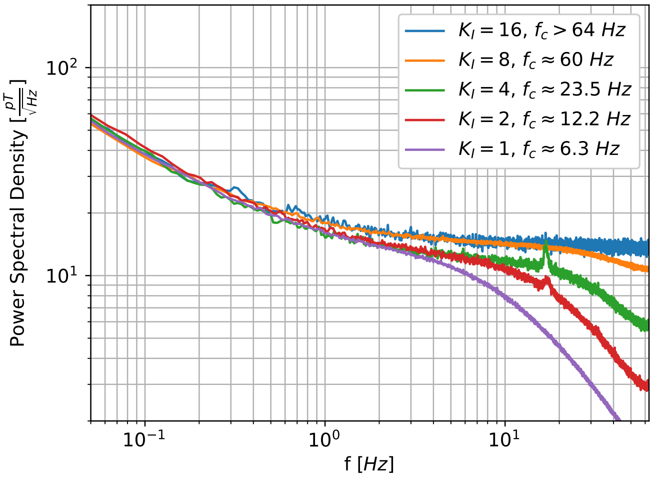

Figure 13. Z-axis noise shapes with different integrator gains in LR mode. A measurement disturbance was recorded at 17 Hz when taking the measurements for integrator gains $K_I = 2$ and $K_I = 4$

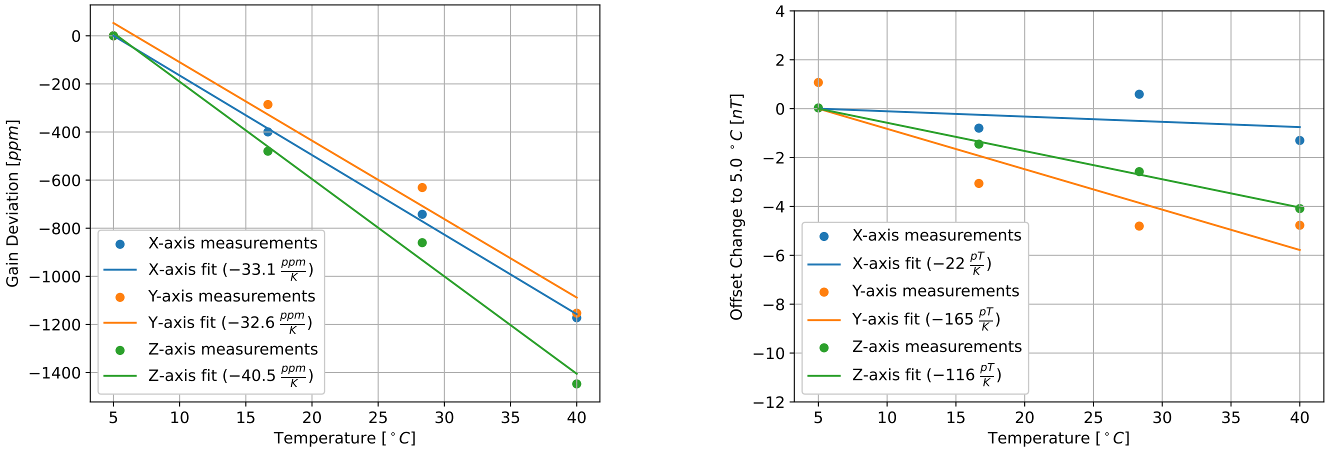

(a) (b)

Figure 14. Sensor Control Unit temperature dependency of the magnetometer LR calibration factors. Left: gain, right: offset

almost four times the temperature coefficient in the opposite direction of the other axes. This may either be a measurement error or be attributed to batch variation of the ASIC lot. The anomalous behavior of this axis is under investigation.

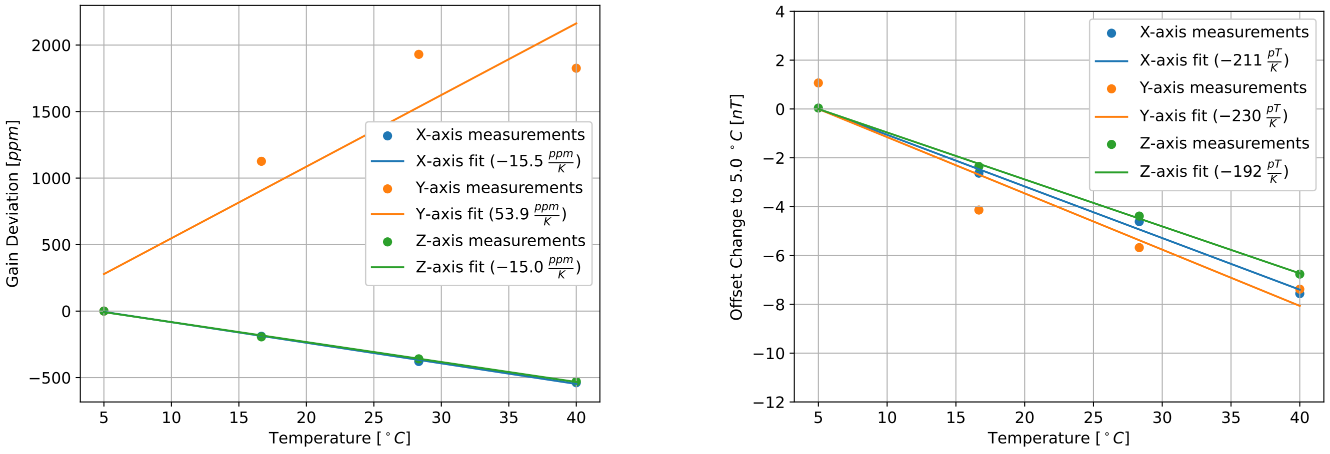

(a) (b)

Figure 15. Temperature dependency of the magnetometer HR calibration factors on sensor control unit temperature. Left: gain, right: offset

While the gain deviation and offset change with respect to temperature can be corrected with a linear fit, the actual measurement is slightly different from this simplification. Table 5 lists the maximum and the root-mean-squared (RMS) of the residuals between the actual measurement and the linear fit. Both the gain deviation and the offset are calculated for both HR and LR

© Author(s) 2026. CC BY 4.0 License.

mode. Nevertheless, these values only provide a first estimation over a limited temperature range and are subject to change in further revisions of the feedback ASIC.

Table 5. Residuals of the Temperature correction fits

Mode	HR				LR			
Parameter	Gain		Offset		Gain		Offset	
Unit	ppm		pT		ppm		pT	
	RMS	max	RMS	max	RMS	max	RMS	max
X	8.11	11.95	227.08	321.15	17.79	29.19	772.70	1092.77
Y	314.55	395.72	974.96	1450.28	60.57	76.67	1043.49	1131.70
Z	6.99	10.83	78.36	108.58	43.44	72.67	83.23	118.65

3.2 Radiation Tests

As the chip was designed for use in space, it has undergone comprehensive radiation testing (Steinhöfler, 2024). This includes investigations of Single-Event Effects (SEE) as well as the response to Total Ionizing Dose (TID). The RADNEXT project (Alía et al., 2023) enabled exposure of the prototype chip to heavy ion irradiation at the Cyclotron Resource Center at the Université catholique de Louvain. A picture of a single feedback ASIC die Device-under-Test (DUT) mounted in the irradiation chamber is shown in Figure 16. In this facility, a cocktail of heavy ions is accelerated in a cyclotron and single species are fired at the die at a defined particle flux. This enables a controlled Linear Energy Transfer (LET) onto the chip, simulating the radiation environment in space.

These heavy ion tests, which induce SEE, have shown that the chip exhibits exceptional hardness against Single-Event Latch-Ups (SEL). Exposure to heavy ions could not trigger a SEL up to LETs of $100\ \frac{\mathrm{MeV\ cm^2}}{\mathrm{mg}}$ (in silicon). This conforms to the expected SEE resilience, as the chip is manufactured in a specialized Complementary Metal-Oxide Semiconductor (CMOS) process that minimizes digital switching noise of logic blocks by embedding logic gate structures into separate semiconducting wells. It is postulated that these wells break up the parasitic thyristor present in traditional CMOS processes, disabling the SEL failure mode.

Nevertheless, Single-Event Transients (SET) and Single-Event Upsets (SEU) were observed. SETs occur in the analog part of the current DAC and cannot be prevented without increasing the power consumption of the chip significantly and/or compromising the noise performance. SETs manifest in the form of a spike in the output current. The appearance of a spike could either be related to an SET in the analog part of the chip or to a SEU in the digital part that is overwritten by follow-up data. A different type of SEUs was traced to the Cascaded Integrator-Comb (CIC) filter that is responsible for up-sampling the input signal. Here, radiation-induced bit flips in the signal registers at the input of one of the integrators of the CIC are permanently stored as a step in the output signal. As seen in Figure 17a, the spike's magnitude covers a substantial part of the output current, while a step appears as a relatively small, but permanent change of the current. However, both happen on small timescales on

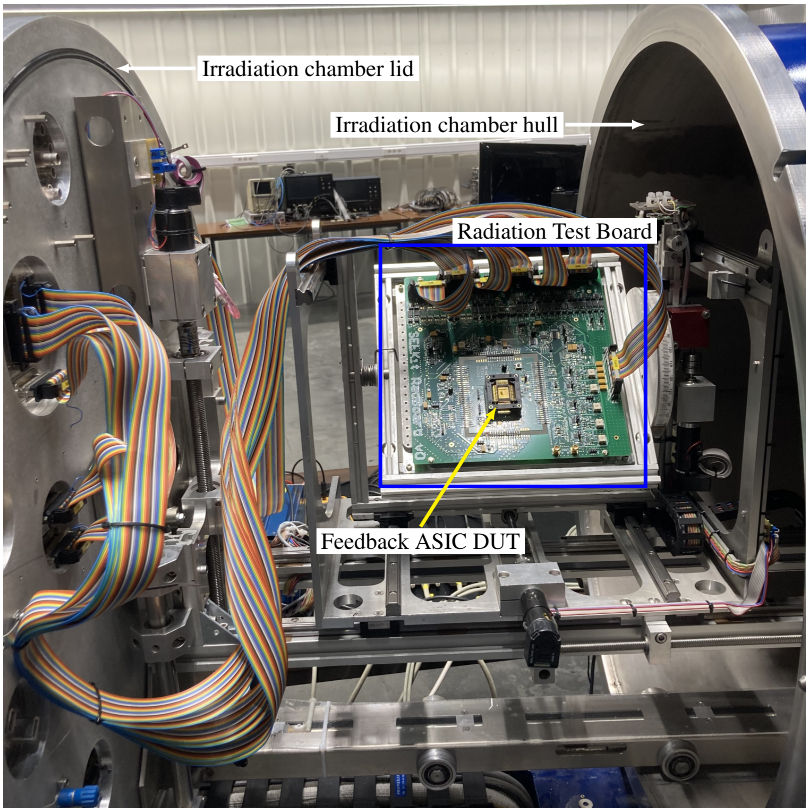

Figure 16. A single Feedback ASIC DUT carried by a radiation test board mounted in the irradiation chamber of the Heavy Ion Facility at the Université catholique de Louvain

the order of 0.5 to 1 ms, which is at the limit of the sampling rate of the test system. Another failure mode was a structured decrease of the output current down to 0. A very typical example is given in Figure 17b. This is classified as a Single-Event Functional Interrupt (SEFI). These SEFIs are also attributed to the CIC, as the decrease shows structured, discrete patterns reminiscent of CIC failure modes.

The susceptibility to SEE is quantitatively described by the SEE cross-section σ_{SEE}, which relates a particle fluence or flux to the number of occurrences or rate of a certain SEE. The LET at which any SEE appears is termed threshold LET LET_{TH}. With increasing LET, the SEE cross-section stops increasing at a certain point. It approaches the saturation cross-section σ_{SAT}. These two fit parameters are pivotal in the design and assessment of a mission with regard to energetic particles. In the post-processing of the data acquired during the irradiation of several DUTs, statistics about the occurrences of the observed SEEs were generated and SEE cross-sections were calculated. For both spikes and steps, a Weibull function was fit to the data, which is shown in Figure 18. The number of observed SEFIs was insufficient to provide a meaningful fit. However, a threshold LET was determined. All the parameters generated by the post-processing are listed in Table 6.

https://doi.org/10.5194/egusphere-2026-1579
Preprint. Discussion started: 15 June 2026
© Author(s) 2026. CC BY 4.0 License.

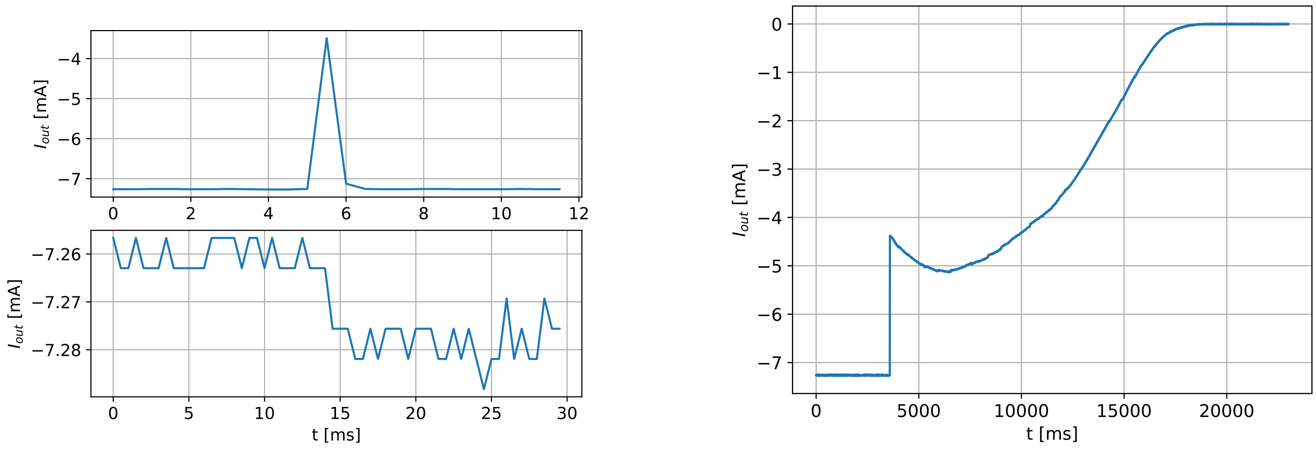

(a)

(b)

Figure 17. Phenomenology of the observed Single-Event Effects. Left: Spike and Step, right: typical functional interrupt

Table 6. Threshold LETs and saturation cross-sections of various SEE in the prototype feedback ASIC

SEE mode	Threshold LET_{TH} $\frac{\mathrm{MeV\ cm}^2}{\mathrm{mg}}$	Saturation cross-section σ_{SAT} cm^2
Spike	11.5	3E-6
Step	14.5	6E-7
SEFI	17	-

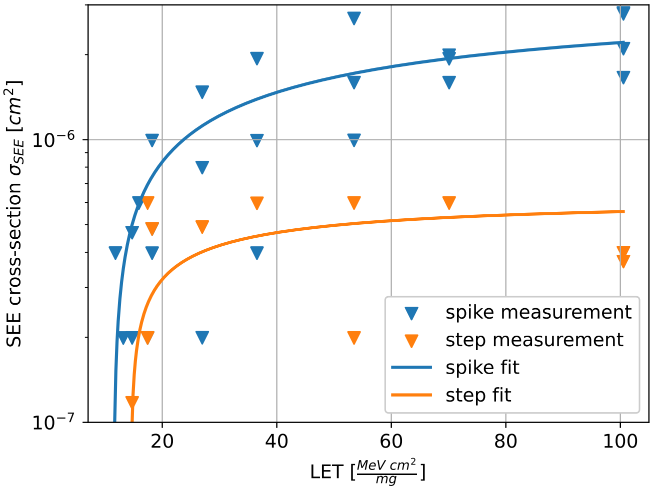

Figure 18. Measured and fitted Single-Event cross-section of both spike and step effects

https://doi.org/10.5194/egusphere-2026-1579
Preprint. Discussion started: 15 June 2026
© Author(s) 2026. CC BY 4.0 License.

As SELs basically do not occur, the feedback ASIC is safe in terms of permanent failure. SETs and SEUs might introduce undesirable degradation of the measurement signal and SEUs and SEFIs are able to cause a state of the ASIC in which it has to be reset to resume operation. However, both SEU and SEFI can be circumvented by introducing redundant logic structures, as they appear in the digital part of the DAC. Techniques such as tripling the signal path and introducing a majority voter circuit can avoid most SEU and SEFI failure modes present in the chip.

In addition, the chip was also tested for TID effects. This test was conducted at the facilities of the Institute for Electronics of Graz University of Technology, where the prototype ASIC was exposed to X-ray radiation, which provides an analog to low energy particles. Figure 19a shows the X-ray irradiation chamber and Figure 19b shows the shielded radiation test board used in these tests.

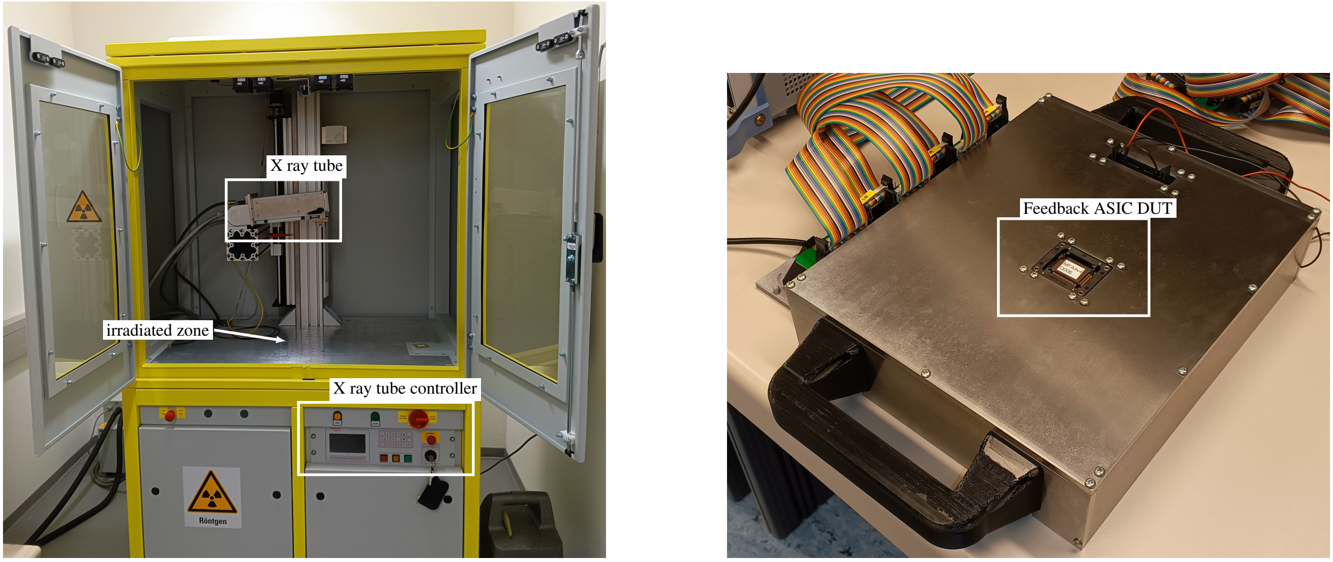

(a)

(b)

Figure 19. X-ray irradiation setup. Left: The irradiation chamber at Graz University of Technology, right: A steel shield protecting the radiation testing electronics while exposing the DUT

During irradiation, it was found that prototype chip remains functional up to high doses beyond the typical values expected for a radiation belt mission. However, the output current generation was still impacted by several effects that became visible with increasing TID. First of all, gain and offset shifts were observed, as shown in Figure 20a and Figure 20b. These shifts do not exhibit a monotonous dependency on the TID applied, meaning that at certain higher doses, the effects seen at lower doses are reversed. Nevertheless, a worst-case deviation from the unirradiated state is estimated and presented. In the relevant range of 0 to 100 krad, the effects of TID on the gain and offset deviation are nearly linear. Within this range, the worst-case deviation is 600 $\frac{\mathrm{ppm}}{\mathrm{krad}}$ for the current output gain and 1 $\frac{\mathrm{\mu A}}{\mathrm{krad}}$ for the current output offset. Higher doses alter the gain and offset further, however the worst-case limit for the gain follows an exponential decay, saturating at a certain value.

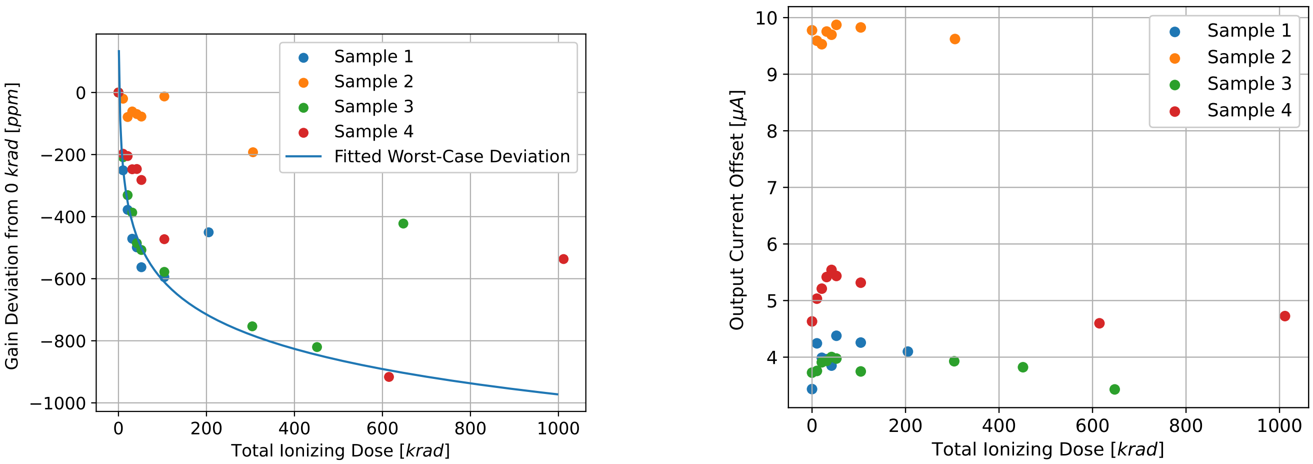

(a)

(b)

Figure 20. Current output deviations induced by Total Ionizing Dose. Left: Relative deviation of the current output's gain factor. An estimation of the worst case is fitted to the data. Right: Absolute deviation of the current output offset

Out of the four samples tested, sample 2 showed a weaker response to the applied dose. This is also visible in the tight clustering of values for sample 2 in Figure 21.

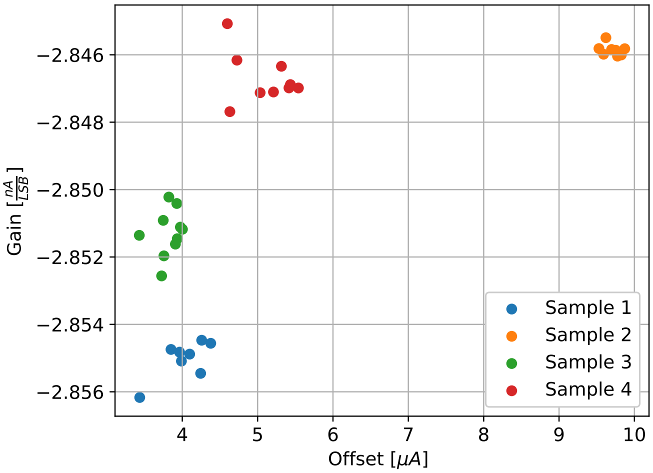

Figure 21. Absolute gain and offset deviation during irradiation up to 1 Mrad

Throughout the irradiation, the basic functionality of the chip remained intact. A total dose of 1 Mrad was tested, exceeding the typical test dose of 100 krad for a radiation belt mission by a factor of 10. In addition to testing functionality, the conducted measurements provide the basis for providing an estimate of the TID-caused measurement error by using the RADFET mea-

© Author(s) 2026. CC BY 4.0 License.

surements on the SCU.

With this high tolerance against TID and SEE, longer in-orbit operation of the instrument becomes possible. Research of the radiation belt dynamics would benefit from these longer time series. Furthermore, current radiation belt knowledge could be extended to periods of high solar activity. The capability of long-term operation, especially during high solar activity periods addresses open points and required observations outlined by the GEM radiation belt focus group (Zhao et al., 2025).

3.3 Discussion of Test Results and Performance comparison

The laboratory tests have shown conclusive results for the noise performance of the instrument, differentiating between the noise contributions of the sensor and both ranges of the sensor control unit. While still 2-3 times higher, the overall noise figure of 20-30 $\frac{\mathrm{pT}}{\sqrt{\mathrm{Hz}}}$ at 1 Hz is in the same order of magnitude as those of big missions such as THEMIS (Auster et al., 2008).

Tests of the effects of temperature on the SCU show the deviations of gain and offset over a temperature range of 5 to 40 °C. The observed effects show a behavior that can be modeled by a linear approximation, enabling simple compensation calculations in the post-processing of measurements. However, bigger temperature ranges will be investigated in future developments.

As evident from the heavy ion irradiation, SEE that may occur during a space mission may introduce spikes, steps and functional interrupts in the measurement. With the determined threshold LET_{TH} and saturation cross-section σ_{SAT}, and the desired mission profile, the expected SEE rate can be determined. Furthermore, the measured TID degradation of the gain and offset of the feedback ASIC can directly be applied as radiation-dependent calibration parameters for the instrument. An envelope for the worst-case gain deviation and offset are given.

A quantitative comparison of key performance parameters is given in Table 7. In this table, the development is compared to state-of the art instruments such as the THEMIS Fluxgate Magnetometer, the fluxgate aboard the Ex-Alta 1 mission (Miles et al., 2016) and the MAGIC magnetoresistive sensor used in the RadCube mission (Eastwood et al., 2025).

Table 7. Comparison of the instrument performance parameters to other missions

Parameter	Unit	THEMIS	Ex-Alta 1	RadCube	this work (HR)	this work (LR)
Range	nT	± 25000	± 65536	± 63000	± 70000	± 23000
Resolution	pT	3	35	114	23	7.6
Noise Floor at 1 Hz	$\frac{pT}{\sqrt{Hz}}$	10	150-200	<500	<30	<20
Mass (excluding boom)	g	375	186	61	215	215
Power Consumption	mW	800	400	480	844	844

https://doi.org/10.5194/egusphere-2026-1579
Preprint. Discussion started: 15 June 2026
© Author(s) 2026. CC BY 4.0 License.

From the table it is evident that the noise and resolution levels of RadCube and Ex-Alta 1 are superseded by this development. Furthermore, the mass of the instrument is comparable and fit for use in a CubeSat. However, higher profile missions such as THEMIS still provide better noise and resolution figures.

The instrument performance is in the range that enables the study of electromagnetic ion cyclotron wave activity, which would not be possible by Ex-Alta 1 and RadCube (Timmermann et al., 2025). This facilitates investigation into wave-particle interaction in the outer radiation belt, as detailed in Yang et al. (2025). Furthermore, applicability to multi-CubeSat radiation belt constellations such as CORBES (Wu et al., 2025) is given with the moderate resource usage. Such missions would greatly benefit from simultaneous high quality measurements in multiple spatial scales. Increased spatio-temporal resolution can help to identify plasma wave power transfer in between the radiation belts (Zhao et al., 2025).

4 Summary and Outlook

In the course of this study, a prototype of a CubeSat-optimized fluxgate magnetometer was designed, built and tested in a laboratory. It comprises a miniaturized three-axis sensor on a deployable boom and a compact Sensor Control Unit with a hybrid feedback ASIC. The prototype delivers low noise while operating over ranges suitable for near-Earth operation, with noise densities of 20–30 $\mathrm{pT}/\sqrt{\mathrm{Hz}}$ (at 1 Hz) and vector ranges of up to ±70µT. The extended housekeeping concept, including an additional auxiliary magnetometer and RADFETs in the Sensor Control Unit, enables disturbance discrimination comparable to the gradiometer approach and provides radiation awareness for operations in harsher environments. With the designed boom, an adequate 65 cm separation of the sensor from the satellite is achieved. Attitude knowledge with an accuracy of 1° is delivered by the boom system while staying within the resource constraints of a 3U–6U CubeSat. With the presented results, it is shown that the instrument is suitable for smaller CubeSat missions requiring high-quality magnetic field measurements.

To reach the performance and robustness demanded by higher-profile missions, several improvements are planned. The next ASIC revision will improve the total ionizing dose response, and reduce temperature sensitivity while increasing reliability through the addition of redundancy in the digital signal processing elements. A subsequent step in development aims to integrate the low-noise amplifiers and analog-to-digital converters into the front-end ASIC, ultimately providing the full sense and path within one chip. This will raise integration density and will further shrink the sensor control unit. A full environmental qualification and in-orbit demonstration will be carried out once this ASIC reaches the desired level of maturity. In parallel, a mechanical qualification of the boom with relevant loads will be completed. This includes deployment reliability, vibration, and dynamic stability testing to characterize settling behavior. With these developments, the instrument will progress from a resource-efficient, CubeSat-ready solution to a mature platform capable of meeting the requirements of more demanding multi-satellite and radiation belt missions.

Author contributions. **Conceptualization:** Raphael Steinhöfler, Marius Anger, Roman Shalamov, Jaan Praks, David Fischer, Aris Valavanoglou; **Data curation:** Raphael Steinhöfler; **Formal analysis:** Raphael Steinhöfler; **Funding acquisition:** Jaan Praks, David Fischer,

Werner Magnes; **Investigation:** Raphael Steinhöfler, Marius Anger, Roman Shalamov, Josef Wilfinger; **Software:** Raphael Steinhöfler, Josef Wilfinger, Constant Lentz; **Supervision:** Jaan Praks, David Fischer, Werner Magnes; **Visualization:** Raphael Steinhöfler, Marius Anger; **Writing – original draft:** Raphael Steinhöfler, Marius Anger; **Writing – review & editing:** Raphael Steinhöfler, Marius Anger, Werner Magnes

Competing interests. The authors declare that they have no financial interests. The authors have no competing interests to declare which are relevant to the content of this article.

Acknowledgements. The presented work was performed as part of and partially financed by the Finnish Centre of Excellence in Research of Sustainable Space (FORESAIL), which is a project under the Research Council of Finland decision numbers **336805** to **336809**.
This activity has received funding from the European Union's 2020 research and innovation programme under grant agreement No **101008126**, corresponding to the RADNEXT project.
We thank Alicja Malgorzata Michalowska-Forsyth and the Institute of Electronics for the exceptional support during the X-ray TID tests.
The authors are grateful for financial support from the Austrian Space Applications Programme (grant nos. **878878**) of the Austrian Research Promotion Agency.

https://doi.org/10.5194/egusphere-2026-1579
Preprint. Discussion started: 15 June 2026
© Author(s) 2026. CC BY 4.0 License.

References

Alía, R. G., Coronetti, A., Bilko, K., Cecchetto, M., Datzmann, G., Fiore, S., and Girard, S.: Heavy Ion Energy Deposition and SEE Intercomparison Within the RADNEXT Irradiation Facility Network, IEEE Transactions on Nuclear Science, 70, 1596–1605, https://doi.org/10.1109/TNS.2023.3260309, 2023.

Anger, M., Niemelä, P., Cheremetiev, K., Clayhills, B., Fetzer, A., Lundén, V., Hiltunen, M., Kärkkäinen, T., Mayank, M., Turc, L., Osmane, A., Palmroth, M., Kilpua, E., Oleynik, P., Vainio, R., Virtanen, P., Toivanen, P., Janhunen, P., Fischer, D., Le Bonhomme, G., Slavinskis, A., and Praks, J.: Foresail-2: Space Physics Mission in a Challenging Environment, Space Science Reviews, 219, 66, https://doi.org/10.1007/s11214-023-01012-7, 2023.

Auster, H. U., Glassmeier, K. H., Magnes, W., Aydogar, O., Baumjohann, W., Constantinescu, D., Fischer, D., Fornacon, K. H., Georgescu, E., Harvey, P., Hillenmaier, O., Kroth, R., Ludlam, M., Narita, Y., Nakamura, R., Okrafka, K., Plaschke, F., Richter, I., Schwarzl, H., Stoll, B., Valavanoglou, A., and Wiedemann, M.: The THEMIS Fluxgate Magnetometer, Space Science Reviews, 141, 235–264, https://doi.org/10.1007/s11214-008-9365-9, 2008.

Balogh, A.: Planetary Magnetic Field Measurements: Missions and Instrumentation, Space Science Reviews, 152, 23–97, https://doi.org/10.1007/s11214-010-9643-1, 2010.

Constantinescu, O. D., Auster, H.-U., Delva, M., Hillenmaier, O., Magnes, W., and Plaschke, F.: Maximum-variance gradiometer technique for removal of spacecraft-generated disturbances from magnetic field data, Geoscientific Instrumentation, Methods and Data Systems, 9, 451–469, https://doi.org/10.5194/gi-9-451-2020, 2020.

Eastwood, J. P., Brown, P., Oddy, T., Archer, M. O., Baughen, R., Belo Ferreira, I., Cobo Torres, C., Cupido, E., Eshbaugh, H., Palla, C., Vitkova, A., Waters, C. L., Whiteside, B., Zabori, B., Hirn, A., Nolbert, D., Milánkovich, D., Kovács, Z. G., Santin, G., and Walker, R.: In Flight Performance of the MAGIC Magnetoresistive Magnetometer on the RadCube CubeSat, Space Science Reviews, 221, 45, https://doi.org/10.1007/s11214-025-01170-w, 2025.

Forslund, Å., Belyayev, S., Ivchenko, N., Olsson, G., Edberg, T., and Marusenkov, A.: Miniaturized digital fluxgate magnetometer for small spacecraft applications, Measurement Science and Technology, 19, 015 202, https://doi.org/10.1088/0957-0233/19/1/015202, 2007.

Holmes-Siedle, A. and Adams, L.: RADFET: A review of the use of metal-oxide-silicon devices as integrating dosimeters, International Journal of Radiation Applications and Instrumentation. Part C. Radiation Physics and Chemistry, 28, 235–244, https://doi.org/10.1016/1359-0197(86)90134-7, 1986.

Miles, D. M., Mann, I. R., Ciurzynski, M., Barona, D., Narod, B. B., Bennest, J. R., Pakhotin, I. P., Kale, A., Bruner, B., Nokes, C. D. A., Cupido, C., Haluza-DeLay, T., Elliott, D. G., and Milling, D. K.: A miniature, low-power scientific fluxgate magnetometer: A stepping-stone to cube-satellite constellation missions, Journal of Geophysical Research: Space Physics, 121, 11,839–11,860, https://doi.org/10.1002/2016JA023147, 2016.

Raman, D. A.: Thermal environment and design considerations of the Foresail-2 satellite mission, Master's thesis, Aalto University, 2023.

Regoli, L. H., Moldwin, M. B., Pellioni, M., Bronner, B., Hite, K., Sheinker, A., and Ponder, B. M.: Investigation of a low-cost magneto-inductive magnetometer for space science applications, Geoscientific Instrumentation, Methods and Data Systems, 7, 129–142, https://doi.org/10.5194/gi-7-129-2018, 2018.

Ripka, P.: Review of fluxgate sensors, Sensors and Actuators A-physical, 33, 129–141, https://api.semanticscholar.org/CorpusID:109837796, 1992.

© Author(s) 2026. CC BY 4.0 License.

Scherzer, M. and Auer, M.: A Digitally-Controlled Fully Differential Low Noise Current Source, in: 2022 IEEE International Symposium on Circuits and Systems (ISCAS), pp. 839–842, https://doi.org/10.1109/ISCAS48785.2022.9937577, 2022.

Scherzer, M., Auer, M., Valavanoglou, A., and Magnes, W.: Implementation of a Fully Differential Low Noise Current Source for Fluxgate Sensors, in: 2022 IEEE 13th Latin America Symposium on Circuits and System (LASCAS), pp. 1–4, https://doi.org/10.1109/LASCAS53948.2022.9789061, 2022.

Steinhöfler, R.: Radiation Evaluation of a Mixed-Signal Application-Specific Integrated Circuit, Master's thesis, Graz University of Technology, 2024.

The CubeSat Program: CubeSat design specification, https://www.cubesat.org/cubesatinfo, 2022.

Timmermann, G., Fischer, D., Auster, H.-U., Richter, I., Grison, B., and Plaschke, F.: Comparison of noise levels of two magnetometer types and their suitability for different space environments, Geoscientific Instrumentation, Methods and Data Systems, 14, 447–458, https://doi.org/10.5194/gi-14-447-2025, 2025.

Vitztum, E., Repän, K., Nemetz, A., Eizinger, M., Baspinar, E. E., Sousanis, A., and Scharlemann, C.: CLIMB—A 3U CubeSat to Van Allen belt, in: Proceedings of the 3rd Symposium on Space Educational Activities (SSEA 2019), Leicester, United Kingdom, https://cubesat.fhwn.ac.at/wp-content/uploads/2020/09/SSEA2019_full_paper_FINAL7.pdf, september 16–18, 2019. Accessed 2026-03-05, 2019.

Wu, J., Deng, L., Praks, J., Anger, M., Oleynik, P., Hajdas, W., Wang, J.-D., Zhang, S.-Y., Zhou, B., Zeng, L., Cao, J., Fischer, D., Liu, S., Chen, W., Wu, F., Xi, R.-C., Li, X., Walter Abrahao, D.-S., Marcos Denardini, C., Li, Y., Yang, X.-C., Dai, L., Ma, Y.-Q., Yu, T., hui Cai, M., Yang, H.-L., Ebrahimi, M., Maurizio, F., Kalegaev, V., Li, W., Miyoshi, Y., Nakamura, R., Petrukovich, A., Baker, D., and Worms, J.-C.: CORBES: Radiation belt survey with international small satellite constellation, Advances in Space Research, 75, 6635–6652, https://doi.org/10.1016/j.asr.2024.04.051, science and applied research with small satellites, 2025.

Yang, X., Li, X., Dai, L., Wu, J., Kalegaev, V., Li, W., Miyoshi, Y., Liu, W., Xiang, Z., Ni, B., Liu, S., Baker, D. N., Wang, C., Deng, L., Li, Y., Praks, J., Anger, M., Wang, J., Zhou, B., Zhang, S., dos Santos, W. A., and Ma, Y.: A multi-satellite survey scheme for addressing open questions on the Earth's outer radiation belt dynamics, Advances in Space Research, 75, 6653–6671, https://doi.org/https://doi.org/10.1016/j.asr.2024.08.008, science and applied research with small satellites, 2025.

Zhao, H., Blum, L., Ukhorskiy, A., and Fu, X.: Community Voices on the Future of Radiation Belt Research: A Summary of the 2024 GEM Radiation Belt Focus Group Round-Table Discussion, Earth and Space Science, 12, e2025EA004 698, https://doi.org/10.1029/2025EA004698, 2025.